

PHOTONICS Research

Polarization assisted self-powered GaN-based UV photodetector with high responsivity

JIAXING WANG,^{1,2,†} CHUNSHUANG CHU,^{1,2,†} KANGKAI TIAN,^{1,2} JIAMANG CHE,^{1,2} HUA SHAO,^{1,2}
YONGHUI ZHANG,^{1,2}  KE JIANG,³  ZI-HUI ZHANG,^{1,2,4}  XIAOJUAN SUN,^{3,5} AND DABING LI³

¹State Key Laboratory of Reliability and Intelligence of Electrical Equipment, Hebei University of Technology, Tianjin 300401, China

²Key Laboratory of Electronic Materials and Devices of Tianjin, School of Electronics and Information Engineering, Hebei University of Technology, Tianjin 300401, China

³State Key Laboratory of Luminescence and Applications, Changchun Institute of Optics, Fine Mechanics and Physics, Chinese Academy of Sciences, Changchun 130033, China

⁴e-mail: zh.zhang@hebut.edu.cn

⁵e-mail: sunxj@ciomp.ac.cn

Received 5 January 2021; revised 22 February 2021; accepted 23 February 2021; posted 23 February 2021 (Doc. ID 418813); published 26 April 2021

In this work, a self-powered GaN-based metal-semiconductor-metal photodetector (MSM PD) with high responsivity has been proposed and fabricated. The proposed MSM PD forms an asymmetric feature by using the polarization effect under one electrode, such that we adopt an AlGaIn/GaN heterojunction to produce the electric field, and by doing so, an asymmetric energy band between the two electrodes can be obtained even when the device is unbiased. The asymmetric feature is proven by generating the asymmetric current-voltage characteristics both in the dark and the illumination conditions. Our results show that the asymmetric energy band enables the self-powered PD, and the peak responsivity wavelength is 240 nm with the responsivity of 0.005 A/W. Moreover, a high responsivity of 13.56 A/W at the applied bias of 3 V is also achieved. Thanks to the very strong electric field in the charge transport region, when compared to the symmetric MSM PD, the proposed MSM PD can reach an increased photocurrent of 100 times larger than that for the conventional PD, even if the illumination intensity for the light source becomes increased. © 2021 Chinese Laser Press

<https://doi.org/10.1364/PRJ.418813>

1. INTRODUCTION

Ultraviolet (UV) detection is an important technology in military and civil applications, such as missile warning, fire monitoring, public security investigation, and environmental detection [1–4]. To achieve UV detection, wide-band-gap semiconductors have to be used, and thus research efforts have been currently devoted to SiC, ZnO, Ga₂O₃, and AlGaIn compounds [5–8]. Among the candidates, AlGaIn-based III-nitride material can be an excellent choice for fabricating UV photodetectors (PDs) owing to the adjustable energy band gap (3.4–6.2 eV), high electron mobility (135–1000 cm²·V^{−1}·s^{−1}), good thermal conductivity (1.3–3.19 W·cm^{−1}·K^{−1}), and excellent chemical stability [9,10]. Based on AlGaIn materials, different PD structures have been developed, e.g., metal-semiconductor-metal (MSM) PDs, Schottky barrier PDs, PIN PDs, and avalanche PDs [11–14]. Among them, AlGaIn-based MSM PDs have attracted significant research attention due to their less complicated fabrication process, low noise, and high detectivity [15]. Conventional MSM PDs use two back-to-back metal-semiconductor contacts to form a symmetric Schottky-type metal/semiconductor struc-

ture [16]. Such design can possess a large absorption region for effectively absorbing photons. However, it is well known that the poor carrier transport efficiency is one of the major limiting factors that hinder the improvement of the photocurrent and responsivity [17]. On one hand, the electric field is generated at the Schottky contact, which is determined by the difference of work functions between the metal and the semiconductor. On the other hand, the limited difference of the work function between the metal and the semiconductor makes the space charge region at the Schottky contact region thin. Therefore, the absence of the electric field in the rest of the optical absorption region strongly hinders the carrier transport, especially when the illumination signal becomes strong. This is because the photogenerated carriers can screen the electric field, which will further reduce the carrier transport between the two Schottky contacts [18,19] and then lead to a saturated photocurrent. The other figure of merit for PDs is that a low dark current is required. For Schottky-contact-based MSM PDs, the leakage current that arises from the thermionic emission at the metal/contact interface cannot be neglected, especially when one metal/semiconductor is reversely biased. Then the image

force at that metal/contact region will cause a reduced barrier height [20], which will inevitably result in the increased leakage current, i.e., the dark current for PDs. Therefore, tremendous effort shall be made to increase the difference between the dark current and the photocurrent so that the enhanced responsivity can be obtained.

An effective method to increase the responsivity is making Schottky contacts with different metals for MSM PDs. Then the different work functions for the two metals will produce the asymmetric energy band, which is very useful to promote the carrier transport. Moreover, such asymmetric energy band profiles can even generate photocurrent when the devices are not biased, i.e., a self-powered MSM PD is achieved [21–25]. One typical AlGaIn-based PD with an asymmetric structure is achieved by using Ni and Au as electrodes at the two ends; the different barrier heights for the Ni/GaN and Au/GaN junctions enable more efficient charge transport and the increased responsivity [22]. However, the responsivity can be further promoted if the energy band can be made more asymmetric. For that purpose, a Pt-Ag GaN MSM PD is reported. The very large potential gradient of 1.39 eV between the Pt and Ag metals then favors the enhanced thermionic emission rate of the electrons for the Pt-Ag MSM PD [21]. A big energy barrier variation can also be obtained by using a Ni-Ti/Al MSM PD structure, and the responsivity of 0.104 A/W can be achieved at the applied bias of 0 V [23]. Other self-powered GaN MSM PDs can also be fabricated by using Ni-Cr Schottky contact pairs and Ni-Ag Schottky contact pairs according to the report in reference [23]. Another MSM PD with the asymmetric structure is achieved by varying the contact area of the Au electrodes [25].

Therefore, our previous literature review shows that, to make self-powered MSM PDs, different Schottky metal contacts shall be used so that the different work functions can produce the asymmetric energy band profiles. Nevertheless, the tilted energy band and the carrier transport are strongly limited by the work function variation for the two Schottky metals. Additionally, the depletion region width that is produced by

the metal/semiconductor structure is small, and this can be easily compensated for by the photogenerated carriers. Then the carrier transport can be strongly affected, especially when the illumination signal is strong enough and the saturation photocurrent might be yielded [26]. In this work, we take the advantage of the polarization effect at the AlGaIn/GaN junction to produce the electric field, i.e., the AlGaIn/GaN junction here imitates the metal-based “Schottky junction.” On one hand, by properly optimizing the epitaxial growth condition, a fully coherent growth mode can be achieved for AlGaIn/GaN heterojunction that is free from strain relaxation. Then the AlGaIn/GaN junction can be fully polarized and the polarization-induced electric field therein will be extremely strong [27]. On the other hand, the polarization-induced electric field cannot be easily screened by free carriers, which promises a high photocurrent even if the detected optical signal intensity is increased.

2. DEVICE ARCHITECTURES AND METHODS

A. Photodetector Design

To address the advantage of our proposed device, we design two device structures as shown in Figs. 1(a) and 1(b). All the layers are epitaxially grown on a *c*-plane sapphire substrate by using a metal organic chemical vapor deposition (MOCVD) system. For Device R, we grow a 4 μm thick undoped GaN absorption layer. For Device N, we further grow a 100 nm thick $\text{Al}_{0.10}\text{Ga}_{0.90}\text{N}$ layer. After the epitaxial growth, Device R is conducted by following the standard fabrication process: 10 nm/10 nm Ni/Au interdigital contacts are deposited by using an e-beam evaporation method. The electrode length, width, and the spacing for the metal contacts are patterned to be 990, 17, and 23 μm , respectively. Then we deposit a 200 nm thick Au layer on the Ni/Au metal stacks for the purpose of a probing test [see Fig. 1(a)]. The additional step for Device N is that we pattern and get the $\text{Al}_{0.10}\text{Ga}_{0.90}\text{N}$ mesa by using dry etching [see Fig. 1(b)]. By doing so, we remove the rest of the $\text{Al}_{0.10}\text{Ga}_{0.90}\text{N}$ layer. Then the same metal deposition

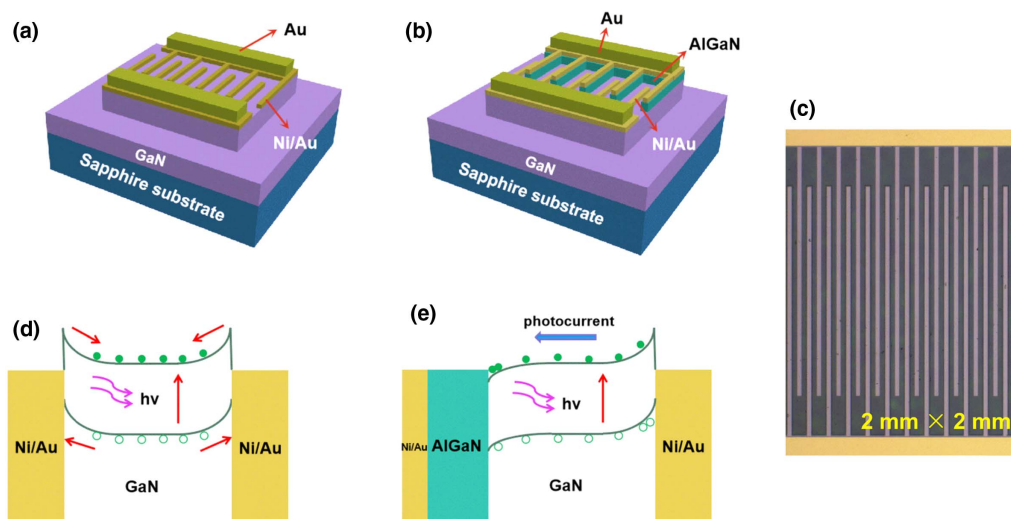


Fig. 1. Schematic structures for (a) Device R and (b) Device N. (c) Top view of GaN-based MSM PD showing interdigital electrodes. Schematic energy band diagrams of (d) Device R and (e) Device N.

processes are conducted as for Device R. Finally, we get the device structure in Fig. 1(c), which shows the interdigital contacts for the $2\text{ mm} \times 2\text{ mm}$ PDs.

Figure 1(d) illustrates the schematic energy band diagrams of the traditional metal/GaN/metal PD structure for Device R. As is shown, the built-in electric fields generated by the two Schottky contacts are of the opposite directions, and the electrons can meet both energy barriers with the same energy barrier height; this energy band profile can strongly hinder the carrier diffusion, and we can also predict no current flow if Device R is not biased. However, when an $\text{Al}_{0.10}\text{Ga}_{0.90}\text{N}$ layer is used under one metal contact, then the very strong polarization-induced electric field can be obtained at the $\text{Al}_{0.10}\text{Ga}_{0.90}\text{N}/\text{GaN}$ interface, which can realign the energy band downwards because of the polarization-induced positive charges at the $\text{Al}_{0.10}\text{Ga}_{0.90}\text{N}/\text{GaN}$ interface [see Fig. 1(e)]. The energy band profile in Fig. 1(e) can also favor the carrier transport, even if Device N is not biased. Our results show that the energy band can be bent by more than 1 eV when a negative bias is applied onto the Schottky metal contact that is fabricated on the GaN layer, which remarkably increases the carrier transport and enhances the photocurrent.

B. Sample Preparation

In the first step, the epilayers of Devices R and N are grown on AlN/sapphire templates by MOCVD. The trimethyl gallium (TMGa), trimethyl aluminum (TMAI), and ammonia (NH_3) are used as the Ga, Al, and N precursors, and hydrogen (H_2) is used as the carrier gas. Through tuning the Al/Ga precursor ratio, the designed Al content can be 0.10 for the AlGa_{0.90}N layer. Next, a device mesa is fabricated by using photolithography and dry etching. The electrodes are prepared by following standard processes of photolithography, e-beam deposition, and lift-off. Finally, the interdigital electrode of 10/10/200 nm Ni/Au/Au is fabricated.

C. Characterizations

The current-voltage curves are measured using a Keithley 6487. The devices are illuminated by monochromatic light from a 266 nm laser on the top side. The incident light power is controlled between 2 and 12 mW in Figs. 2(b) and 2(c). The diameter of the incident laser spot is 3 mm. The spectral responses are measured by a DSR100 system with a xenon lamp, chopper, monochromator, Keithley 6487, SR830 lock-in amplifier, and standard Si detector. All response spectra have been calibrated by the standard Si detector. The transient response spectra are measured by a RIGOL DS6104 digital oscilloscope. A pulsed laser with the wavelength of 266 nm is used to measure the photocurrent and transient responses.

D. Simulations

The APSYS calculations are carried out with a commercial software: Crosslight Software Inc. APSYS 2018 (<http://www.crosslight.com>), which can solve the continuity equation and Poisson equation by using the finite element method. The drift and diffusion processes for carriers can also be considered. The Shockley–Read–Hall (SRH) recombination lifetime is set to 10 ns [28]. The electron affinity for the Ni is set to 5.15 eV [29]. The polarization effect is considered at the $\text{Al}_{0.10}\text{Ga}_{0.90}\text{N}/\text{GaN}$ heterojunction, and the polarization

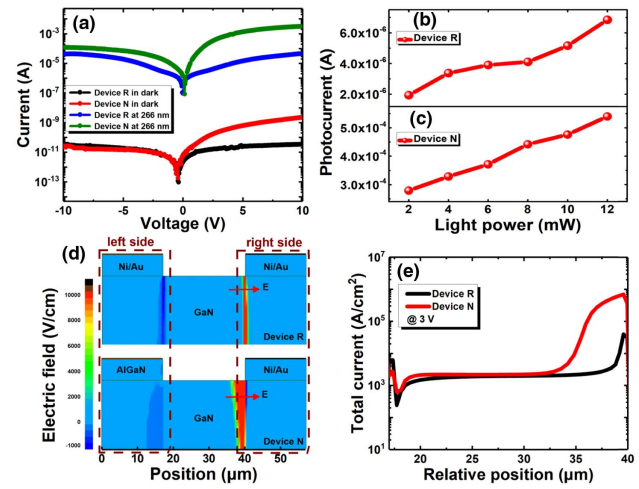


Fig. 2. (a) Dark current and photocurrent in terms of the applied bias for Devices R and N. Photocurrent for (b) Device R and (c) Device N in terms of different laser powers. (d) Two-dimensional electric field profiles and (e) current distributions for Devices R and N at the applied bias of 3 V under the 266 nm UV illumination. The bias is applied at the left electrode, such that the positive bias is biased at the left electrode in the first quadrant and the negative bias is biased at the left electrode in the second quadrant. The other electrode is grounded when the devices are measured. The wavelength for the illumination laser is 266 nm. The positive direction for the electric field is defined to point to the right side in (d).

Table 1. Absorption Coefficient of GaN Under Different Wavelengths

Wavelength (nm)	Absorption Coefficient (m^{-1})
250	3.355×10^7
260	3.140×10^7
270	2.927×10^7
280	2.714×10^7
290	2.500×10^7
300	2.283×10^7
310	2.058×10^7
320	1.823×10^7
330	1.570×10^7
340	1.287×10^7
350	9.459×10^6
360	4.189×10^6
370	1.704×10^5
380	6.500×10^3
390	2.933×10^2
400	1.545×10^1

charge density is set to $\sim 3.97 \times 10^{16} \text{ m}^{-2}$ [30]. The energy band offset for the $\text{Al}_{0.10}\text{Ga}_{0.90}\text{N}/\text{GaN}$ junction is set to 50/50 [31]. The absorption coefficient for GaN in terms of the wavelength can be found in Table 1 [32]. Other parameters regarding nitride semiconductors can be found elsewhere [33].

3. RESULTS AND DISCUSSION

The dark current and the photocurrent as functions of the applied bias for the as-fabricated GaN-based MSM PDs are presented in Fig. 2(a). The bias is applied at the left elec-

trode, such that the positive bias is biased at the left electrode in the first quadrant and the negative bias is biased at the left electrode in the second quadrant. The other electrode is grounded when the devices are measured. We have observed symmetric current-voltage characteristics for Device R, which agree with the energy band profile in Fig. 1(d). Nevertheless, the asymmetric current in terms of the applied bias is obtained for Device N, which is a signature for the unbalanced energy band profile as indicated in Fig. 1(e). The dark current for Device N is larger than that for Device R in the first quadrant, which means that the polarized $\text{Al}_{0.10}\text{Ga}_{0.90}\text{N}/\text{GaN}$ interface can increase the electric field in the GaN absorption layer. This can promote the drift and diffusion for carriers. However, the dark current for the two devices shows negligible difference in the second quadrant, which indicates the similar Schottky barrier height for the Ni/Au/GaN structure. This also means that the metal deposition process for our devices is stable. When the devices are illuminated under the 266 nm laser diode, both devices generate photocurrent with the higher photocurrent level for Device N, especially in the first quadrant. The much more enhanced photocurrent for Device N in the first quadrant is mainly attributed to the polarized $\text{Al}_{0.10}\text{Ga}_{0.90}\text{N}/\text{GaN}$ interface. The photocurrent for Device N is also slightly larger than that for Device R in the second quadrant, which is likely due to the hole trapping effect [22], such that we get the $\text{Al}_{0.10}\text{Ga}_{0.90}\text{N}$ mesa by using dry etching, and this can produce traps on the GaN surface for trapping holes. Then the electrons will be less recombined with holes and can contribute to the drift and diffusion current. Figures 2(b) and 2(c) show the photocurrent for Devices R and N under different laser powers, and we can see that the photocurrent for Device N is always higher than that for Device R, which infers that Device N can more accurately detect the very strong optical signal without photocurrent saturation. Note that we are not able to further increase the optical signal power because of the limited laser power. To even better demonstrate the origin of the enhanced photocurrent for Device N, we calculate and present the two-dimensional electric field profiles between the two electrodes in Fig. 2(d). The positive direction for the electric field is defined to point to the right side [see the arrows in Fig. 2(d)]. When we look at the

right sides of the devices, we find that, thanks to the polarized $\text{Al}_{0.10}\text{Ga}_{0.90}\text{N}/\text{GaN}$ interface, the generated electric field for Device N is larger than that for Device R. When we investigate the left sides of the devices, the electric field is negative, i.e., it points to the left side for both devices. However, the electric field for the horizontal component therein is smaller for Device N (-80 V/cm) than that for Device R ($-2.5 \times 10^3 \text{ V/cm}$). The smaller electric field intensity for Device N at the left side arises from the screening effect by the polarization-induced positive charges at the $\text{Al}_{0.10}\text{Ga}_{0.90}\text{N}/\text{GaN}$ interface. The electric field profile for Device N can even better favor the carrier transport, which is further evidenced in Fig. 2(e). We can intuitively see that the current for Device N is higher than that for Device R, especially in the region from 33 to $40 \mu\text{m}$. It indicates that we require a strong electric field in the optical absorption region so that the photogenerated carriers can be more effectively moved between the two metal electrodes.

Then we probe the responsivity when the devices are not biased. According to our previous analysis, the carrier movement requires the potential difference between the two ends. The symmetrical energy band profiles for the conventional GaN PD, i.e., Device R in this work, cannot support the carrier transport without external electric bias. However, the polarized $\text{Al}_{0.10}\text{Ga}_{0.90}\text{N}/\text{GaN}$ interface enables our proposed Device N to have the potential difference, and the carriers can transport between the two electrodes even if the device is not biased. We then measure the responsivity for Devices R and N at the applied bias of 0 V in Fig. 3(a). When compared with Device R, Device N shows a self-powered feature such that the peak responsivity of 0.005 A/W is obtained at the solar blind wavelength of 240 nm. The cutoff wavelength is 360 nm, which corresponds to the energy band gap for the GaN layer. Note that this solar blind signal might be caused by the $\text{Al}_{0.10}\text{Ga}_{0.90}\text{N}$ layer when the light is reflected by the GaN layer and reaches the $\text{Al}_{0.10}\text{Ga}_{0.90}\text{N}$ mesa edge. Moreover, according to Table 1, GaN also has a high absorption coefficient in the solar blind spectral range, while the polarization field in the GaN layer further favors the generation of the peak responsivity at 240 nm. Meanwhile, the rejection ratios of Devices R and N

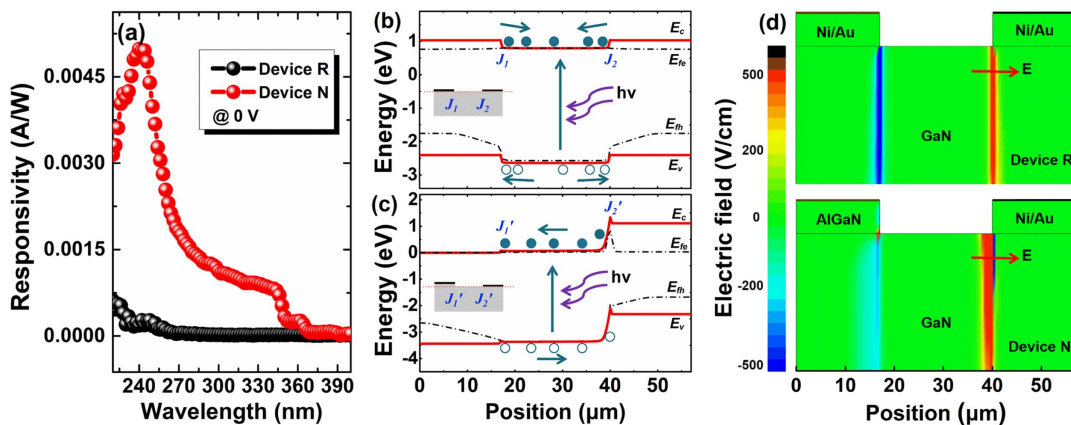


Fig. 3. (a) Spectral responsivity, (b) and (c) energy band diagrams near the GaN layer surface, and (d) two-dimensional electric field profiles for Devices R and N at the applied bias of 0 V under 266 nm UV illumination. E_c , E_v , E_{fc} , and E_{fv} denote energies of the conduction band, the valence band, and quasi-Fermi levels for electrons and holes, respectively. The positive direction for the electric field is defined to point to the right side in (d).

are 35.73 and 97.95 at 0 V bias, respectively. Here the rejection ratio is defined as $R_{\text{peak}}/R_{390\text{ nm}}$. Here R_{peak} and $R_{390\text{ nm}}$ represent the peak responsivity and the responsivity at 390 nm. We can see that the rejection ratio of Device N is higher than that of Device R.

In order to reveal the origin of the responsivity for Device N, we calculate and show the energy band diagrams for Devices R and N under 266 nm UV light illumination in Figs. 3(b) and 3(c), respectively. Note that both devices are not biased. In Fig. 3(b), we define two metal-semiconductor junctions as J_1 and J_2 for Device R. Similarly, J'_1 and J'_2 are also defined for the $\text{Al}_{0.10}\text{Ga}_{0.90}\text{N}/\text{GaN}$ junction and metal-semiconductor junction for Device N in Fig. 3(c), respectively. When the two devices are illuminated by the 266 nm UV light, electron-hole pairs are generated in the GaN absorption layer. For Device R, the same energy barrier can be observed at J_1 and J_2 . Therefore, the photogenerated electrons will be confined in the region with lower conduction band energy. Although the holes are located at the valence band with high energy, the low hole mobility will still localize most holes in the GaN absorption region. If we look into the calculated energy band for Device N in Fig. 3(c), we can see that the energy band is strongly bent. The photogenerated electrons experience potential variation between J'_1 and J'_2 , and the potential difference provides the kinetic energy for both electrons and holes. Then the electrons and holes can overcome the barrier height at the $\text{Ni}/\text{Al}_{0.10}\text{Ga}_{0.90}\text{N}/\text{GaN}$ junction and the Ni/GaN junction, respectively. As a result, the photocurrent is produced and we detect the responsivity when the applied bias is 0 V for Device N. The calculated two-dimensional electric field profiles for Devices R and N under the 266 nm UV illumination are also given in Fig. 3(d). The electric field profiles are consistent with

the energy band alignments for Devices R and N, respectively. The direction of the electric field at the position of J_1 is opposite to that at the position of J_2 , while the electric field intensity is the same. It means that the net electric field is neutralized. Therefore, neither electrons nor holes can freely move between the two metal electrodes. On the other hand, although the directions for the electric field at positions of J'_1 and J'_2 oppose to each other, the electric field intensity at the position of J'_2 is larger than that at the position of J'_1 . Therefore, the electrons and holes can be pushed to obtain movement between the two metal contacts. These presented results indicate a promising and simple method to fabricate excellent self-powered GaN-based PD by using the inherent polarization effect for III-nitride-based compounds.

The responsivity as a function of wavelength at different applied biases for Devices R and N is shown in Figs. 4(a) and 4(b), respectively. As the applied bias increases from 0 to 3 V, the value of responsivity for both devices increases. However, the responsivity for Device R is always lower than that for Device N. Device R shows the peak responsivity of 0.078 A/W at the wavelength of 360 nm. A sharp cutoff in the responsivity can be observed when the wavelength of the light is beyond 360 nm, which corresponds to the band gap of GaN [22,34]. For Device N, the peak responsivity is 13.56 A/W at the applied bias of 3 V, which is 170 times larger than that for Device R. The increased responsivity for Device N is tentatively attributed to the stronger polarization-induced electric field in the GaN absorption layer, which makes the carriers more efficiently drift between the two metal electrodes. It is worth noting that this peak wavelength shows a blueshift for Device N when compared to Device R, which may be due to the absorption of the $\text{Al}_{0.10}\text{Ga}_{0.90}\text{N}$ layer.

A comparative chart is presented in Table 2, which summarizes the responsivity and peak wavelength for the reported GaN-based MSM PDs. It shows that the highest responsivity of 10^6 A/W is at the peak wavelength of 250 nm according to Ref. [35]. However, the self-powered mode cannot be achieved. Our peak responsivity of 13.56 A/W with an on/off ratio of 10^6 at the wavelength of 346 nm and the self-powered detection capability can be simultaneously achieved. Therefore, our design can realize both the high responsivity and the self-powered detection capability, proving the advantage of the polarization effect for improving the GaN-based

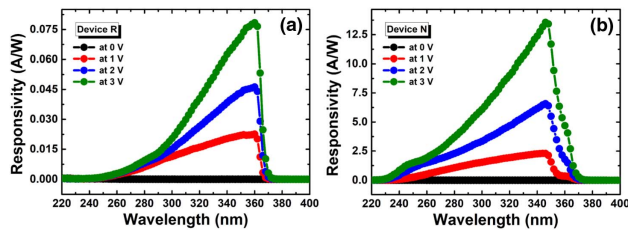


Fig. 4. Spectral responsivity for (a) Device R and (b) Device N at different applied biases.

Table 2. Performances for the Reported GaN-Based and AlGaIn-Based PDs in the Literature

Material	Responsivity	Wavelength (nm)	Self-powered	On/Off Ratio	Year	Refs.
GaN	0.00154 A/W at 0 V	340	Yes	—	2016	[36]
GaN	3.096 A/W at 10 V	360	No	10^6	2017	[16]
$\text{Al}_{0.6}\text{Ga}_{0.4}\text{N}/\text{Al}_{0.5}\text{Ga}_{0.5}\text{N}$	10^6 A/W at 5 V	250	No	5×10^6	2017	[35]
GaN	0.28 A/W at 10 V	325	Yes	<10	2018	[37]
AlGaIn	0.115 A/W at 0 V, 0.154 A/W at 3 V	270	Yes	—	2018	[38]
GaN	0.633 A/W at 5 V	325	Yes	<10	2018	[21]
$\text{Al}_{0.4}\text{Ga}_{0.6}\text{N}$	0.30 A/W at 8 V	265	No	10^6	2019	[2]
GaN	0.147 A/W at 3 V	368	No	10^4	2019	[39]
Ultra-thin GaN	0.00176 A/W at 0 V	325	Yes	<10	2020	[26]
$\text{Al}_{0.45}\text{Ga}_{0.65}\text{N}$	3.10 A/W at 30 V	250	No	10^4	2020	[40]
GaN	0.005 A/W at 0 V, 13.56 A/W at 3 V	346	Yes	10^6	2021	This work

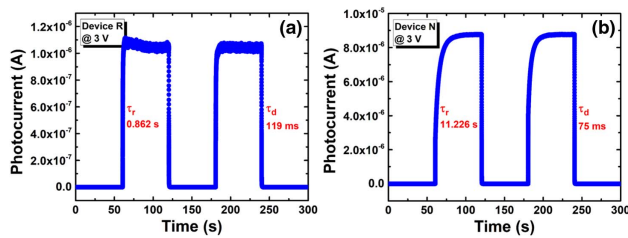


Fig. 5. Time-dependent photo-response characteristics for (a) Device R and (b) Device N when devices are biased to 3 V. The laser wavelength is 266 nm.

PD performance. Furthermore, our design can detect the solar blind wavelength range of 240 nm in the self-powered mode.

It is well known that the response speed of PDs is strongly related to the carrier transport and carrier collection. To study the photo-response time for the two investigated devices, the time-dependent photo responses for Devices R and N are measured under the illumination of the 266 nm laser signal in Figs. 5(a) and 5(b), respectively. The devices are biased at 3 V. Both devices exhibit the on and off states with the laser signal, meaning the carriers can be generated and decayed when the laser is turned on and off, respectively. Device R shows a rise time (τ_r) of 0.862 s and a decay time (τ_d) of 119 ms. Here τ_r is defined as the time interval when the photocurrent increases from 10% to 90% of its peak value. τ_d is defined as the time interval when the photocurrent decreases from 90% to 10% of its peak value [41]. τ_r and τ_d for Device N are estimated to 11.226 s and 75 ms, respectively. Obviously, τ_r for Device N is much longer than that for Device R, but τ_d for Device N is shorter than that for Device R. The much increased τ_r for Device N can be attributed to the photoconductive mode, such that the dry etching process may produce traps on the GaN surface, and then the hole trapping effect prevents the electrons from being recombined with holes [22]. Thus, the longer τ_r for Device N is obtained. When the laser is switched off, the much stronger electric field can quickly sweep the photogenerated carriers from the GaN absorption layer to the metal electrodes, which leads to the shorter τ_d for Device N. It is also worth noting that the photoconductive mode can also prolong the falling time [42]. Therefore, we believe that in our case the carrier sweeping effect for Device N shall dominate the decay process. We also believe that such slow response can be improved by surface passivation. The improvement of response speed might sacrifice responsivity. Therefore, to increase the responsivity, we can increase the light absorption capability by reducing the optical reflection at the GaN surface, which may be achieved by fabricating nanopatterns by using nano-imprint or holographic lithography processes.

4. CONCLUSIONS

In conclusion, we demonstrate the fabrication and the characterization of a self-powered GaN-based MSM UV PD. The self-powered GaN UV PD is realized by using the polarized $\text{Al}_{0.10}\text{Ga}_{0.90}\text{N}/\text{GaN}$ interface, and the polarization-induced electric field can produce the asymmetric energy band. Then, photogenerated carriers can be transported even if the device is

not biased, and peak responsivity as high as 0.005 A/W is obtained at the solar blind wavelength of 240 nm. Moreover, the potential difference between the two metal electrodes is further proven by showing the asymmetric dark current and photocurrent in terms of the applied bias for Device N. Our measurement also demonstrates a high responsivity of 13.56 A/W at the applied bias of 3 V bias for the proposed structure. The photoconductive mode is also observed by showing the increased rise time when the time-dependent photo response is measured for Device N, which can be another possible reason for the very high photocurrent and the responsivity. However, the stronger electric field can make the carriers swept out of the GaN absorption layer rapidly, and hence a faster decay time is obtained for Device N. Thus, plenty of research effort shall also be made to achieve both the high responsivity and the fast photo-response capability. Therefore, this study provides a feasible and cost-effective route for designing GaN-based self-powered MSM UV detectors with very high responsivity. We strongly believe that the reported structures are very useful for the community to make high-performance GaN-based UV detectors, and the device physics revealed here enriches the understanding of photosensitive devices.

Funding. State Key Laboratory of Reliability and Intelligence of Electrical Equipment, Hebei University of Technology (EERI_PI2020008); National Natural Science Foundation of China (61725403, 61922978, 62074050).

Disclosures. The authors declare no conflicts of interest related to this paper.

[†]These authors contributed equally to this work.

REFERENCES

1. L. Ravikiran, K. Radhakrishnan, N. Dharmarasu, M. Agrawal, Z. Wang, A. Bruno, C. Soci, T. Lihuang, and K. S. Ang, "GaN Schottky metal-semiconductor-metal UV photodetectors on Si(111) grown by ammonia-MBE," *IEEE Sens. J.* **17**, 72–77 (2017).
2. N. Lu, Y. Gu, Y. Weng, Z. Da, and Y. Ding, "Localized surface plasmon enhanced photoresponse of AlGaIn MSM solar-blind ultraviolet photodetectors," *Mater. Res. Express* **6**, 095033 (2019).
3. S. F. Chichibu, K. Shima, K. Kojima, S. Takashima, K. Ueno, M. Edo, H. Iguchi, T. Narita, K. Kataoka, S. Ishibashi, and A. Uedono, "Room temperature photoluminescence lifetime for the near-band-edge emission of epitaxial and ion-implanted GaN on GaN structures," *Jpn. J. Appl. Phys.* **58**, SC0802 (2019).
4. M. Razeghi and A. Rogalski, "Semiconductor ultraviolet detectors," *J. Appl. Phys.* **79**, 7433–7473 (1996).
5. T. Yang, S. Chen, X. Li, X. Xu, F. Gao, L. Wang, J. Chen, W. Yang, X. Hou, and X. Fang, "High-performance SiC nanobelt photodetectors with long-term stability against 300°C up to 180 days," *Adv. Funct. Mater.* **29**, 1806250 (2019).
6. Z. Xu, Y. Zhang, and Z. Wang, "ZnO-based photodetector: from photon detector to pyro-phototronic effect enhanced detector," *J. Phys. D* **52**, 223001 (2019).
7. J. Wang, L. Ye, X. Wang, H. Zhang, L. Li, C. Kong, and W. Li, "High transmittance $\beta\text{-Ga}_2\text{O}_3$ thin films deposited by magnetron sputtering and post-annealing for solar-blind ultraviolet photodetector," *J. Alloy. Compd.* **803**, 9–15 (2019).
8. X. Li, C. Hemmingsson, U. Forsberg, E. Janzén, and G. Pozina, "Optical properties of AlGaIn/GaN epitaxial layers grown on different face GaN substrates," *Mater. Lett.* **263**, 127229 (2020).

9. Z. Alaie, S. M. Nejad, and M. H. Yousefi, "Recent advances in ultraviolet photodetectors," *Mater. Sci. Semicond. Process.* **29**, 16–55 (2015).
10. M. Zhang, Y. Wang, F. Teng, L. Chen, J. Li, J. Zhou, X. Pan, and E. Xie, "A photoelectrochemical type self-powered ultraviolet photodetector based on GaN porous films," *Mater. Lett.* **162**, 117–120 (2016).
11. A. Müller, G. Konstantinidis, M. Androulidaki, A. Dinescu, A. Stefanescu, A. Cismaru, D. Neculoiu, E. Pavelescu, and A. Stavrinidis, "Front and backside-illuminated GaN/Si based metal-semiconductor-metal ultraviolet photodetectors manufactured using micromachining and nano-lithographic technologies," *Thin Solid Films* **520**, 2158–2161 (2012).
12. W. Mou, L. Zhao, L. Chen, D. Yan, H. Ma, G. Yang, and X. Gu, "GaN-based Schottky barrier ultraviolet photodetectors with graded doping on patterned sapphire substrates," *Solid-State Electron.* **133**, 78–82 (2017).
13. G. Wang, H. Lu, D. Chen, F. Ren, R. Zhang, and Y. Zheng, "High quantum efficiency GaN-based p-i-n ultraviolet photodetectors prepared on patterned sapphire substrates," *IEEE Photon. Technol. Lett.* **25**, 652–654 (2013).
14. F. Wang, "Theoretical study of back-illuminated separated absorption and multiplication AlGaIn APDs with different structural parameters," *Opt. Quantum Electron.* **49**, 216 (2017).
15. A. Gundimeda, S. Krishna, N. Aggarwal, A. Sharma, N. D. Sharma, K. K. Maurya, S. Husale, and G. Gupta, "Fabrication of non-polar GaN based highly responsive and fast UV photodetector," *Appl. Phys. Lett.* **110**, 103507 (2017).
16. S. Chang, M. Chang, and Y. Yang, "Enhanced responsivity of GaN metal-semiconductor-metal (MSM) photodetectors on GaN substrate," *IEEE Photon. J.* **9**, 6801707 (2017).
17. S. Rathkanthiwar, A. Kalra, S. V. Solanke, N. Mohta, R. Muralidharan, S. Raghavan, and D. N. Nath, "Gain mechanism and carrier transport in high responsivity AlGaIn-based solar blind metal semiconductor metal photodetectors," *J. Appl. Phys.* **121**, 164502 (2017).
18. T. H. Wood, J. Z. Pastalan, C. A. Burrus, B. C. Johnson, B. I. Miller, J. L. deMiguel, U. Koren, and M. G. Young, "Electric field screening by photogenerated holes in multiple quantum wells: a new mechanism for absorption saturation," *Appl. Phys. Lett.* **57**, 1081–1083 (1990).
19. K. Shimomura, "Proposal of field-effect-type photodetector using field-screening effect in the absorption of light," *Jpn. J. Appl. Phys.* **31**, L1757–L1759 (1992).
20. F. Xie, H. Lu, X. Xiu, D. Chen, P. Han, R. Zhang, and Y. Zheng, "Low dark current and internal gain mechanism of GaN MSM photodetectors fabricated on bulk GaN substrate," *Solid-State Electron.* **57**, 39–42 (2011).
21. S. K. Jain, S. Krishna, N. Aggarwal, R. Kumar, A. Gundimeda, S. C. Husale, V. Gupta, and G. Gupta, "Effect of metal contacts on a GaN/sapphire-based MSM ultraviolet photodetector," *J. Electron. Mater.* **47**, 6086–6090 (2018).
22. D. Li, X. Sun, H. Song, Z. Li, H. Jiang, Y. Chen, G. Miao, and B. Shen, "Effect of asymmetric Schottky barrier on GaN-based metal-semiconductor-metal ultraviolet detector," *Appl. Phys. Lett.* **99**, 261102 (2011).
23. X. Sun, D. Li, Z. Li, H. Song, H. Jiang, Y. Chen, G. Miao, and Z. Zhang, "High spectral response of self-driven GaN-based detectors by controlling the contact barrier height," *Sci. Rep.* **5**, 16819 (2015).
24. M. Casalino, M. Iodice, L. Sirleto, I. Rendina, and G. Coppola, "Asymmetric MSM sub-bandgap all-silicon photodetector with low dark current," *Opt. Express* **21**, 28072–28082 (2013).
25. L. Dong, J. Yu, R. Jia, J. Hu, Y. Zhang, and J. Sun, "Self-powered MSM deep-ultraviolet β -Ga₂O₃ photodetector realized by an asymmetrical pair of Schottky contacts," *Opt. Mater. Express* **9**, 1191–1199 (2019).
26. L. Goswami, R. Pandey, and G. Gupta, "Ultra-thin GaN nanostructures based self-powered ultraviolet photodetector via non-homogeneous Au-GaN interfaces," *Opt. Mater.* **102**, 109820 (2020).
27. T. Kabemura, S. Ueda, Y. Kawada, and K. Horio, "Enhancement of breakdown voltage in AlGaIn/GaN HEMTs: field plate plus high-k passivation layer and high acceptor density in buffer layer," *IEEE Trans. Electron Devices* **65**, 3848–3854 (2018).
28. Z.-H. Zhang, S.-W. Huang Chen, Y. Zhang, L. Li, S.-W. Wang, K. Tian, C. Chu, M. Fang, H.-C. Kuo, and W. Bi, "Hole transport manipulation to improve the hole injection for deep ultraviolet light-emitting diodes," *ACS Photon.* **4**, 1846–1850 (2017).
29. N. Miura, T. Nanjo, M. Suita, T. Oishi, Y. Abe, T. Ozeki, H. Ishikawa, T. Egawa, and T. Jimbo, "Thermal annealing effects on Ni/Au based Schottky contacts on n-GaN and AlGaIn/GaN with insertion of high work function metal," *Solid-State Electron.* **48**, 689–695 (2004).
30. M. Brendel, M. Helbling, A. Knigge, F. Brunner, and M. Weyers, "Measurement and simulation of top- and bottom-illuminated solar-blind AlGaIn metal-semiconductor-metal photodetectors with high external quantum efficiencies," *J. Appl. Phys.* **118**, 244504 (2015).
31. Z.-H. Zhang, L. Li, Y. Zhang, F. Xu, Q. Shi, B. Shen, and W. Bi, "On the electric-field reservoir for III-nitride based deep ultraviolet light-emitting diodes," *Opt. Express* **25**, 16550–16559 (2017).
32. J. F. Muth, J. D. Brown, M. A. L. Johnson, Z. Yu, R. M. Kolbas, J. W. Cook, and J. F. Schetzina, "Absorption coefficient and refractive index of GaN, AlN and AlGaIn alloys," *MRS Internet J. Nitride Semicond. Res.* **4**, 502–507 (1999).
33. D. Li, K. Jiang, X. Sun, and C. Guo, "AlGaIn photonics: recent advances in materials and ultraviolet devices," *Adv. Opt. Photon.* **10**, 43–110 (2018).
34. X. Sun, D. Li, H. Jiang, Z. Li, H. Song, Y. Chen, and G. Miao, "Improved performance of GaN metal-semiconductor-metal ultraviolet detectors by depositing SiO₂ nanoparticles on a GaN surface," *Appl. Phys. Lett.* **98**, 121117 (2011).
35. A. Yoshikawa, S. Ushida, K. Nagase, M. Iwaya, T. Takeuchi, S. Kamiyama, and I. Akasaki, "High-performance solar-blind Al_{0.6}Ga_{0.4}N/Al_{0.5}Ga_{0.5}N MSM type photodetector," *Appl. Phys. Lett.* **111**, 191103 (2017).
36. N. Prakash, M. Singh, G. Kumar, A. Barvat, K. Anand, P. Pal, S. P. Singh, and S. P. Khanna, "Ultrasensitive self-powered large area planar GaN UV-photodetector using reduced graphene oxide electrodes," *Appl. Phys. Lett.* **109**, 242102 (2016).
37. S. K. Jain, N. Aggarwal, S. Krishna, R. Kumar, S. Husale, V. Gupta, and G. Gupta, "GaN-UV photodetector integrated with asymmetric metal semiconductor metal structure for enhanced responsivity," *J. Mater. Sci. Mater. Electron.* **29**, 8958–8963 (2018).
38. W. Y. Han, Z. W. Zhang, Z. M. Li, Y. R. Chen, H. Song, G. Q. Miao, F. Fan, H. F. Chen, Z. Liu, and H. Jiang, "High performance back-illuminated MIS structure AlGaIn solar-blind ultraviolet photodiodes," *J. Mater. Sci. Mater. Electron.* **29**, 9077–9082 (2018).
39. Y. P. Chen, C. H. Zheng, L. Q. Hu, and Y. R. Chen, "Improved performance of a back-illuminated GaN-based metal-semiconductor-metal ultraviolet photodetector by *in-situ* modification of one-dimensional ZnO nanorods on its screw dislocations," *J. Alloy. Compd.* **775**, 1213–1220 (2019).
40. K. Jiang, X. Sun, Z.-H. Zhang, J. Ben, J. Che, Z. Shi, Y. Jia, Y. Chen, S. Zhang, W. Lv, and D. Li, "Polarization-enhanced AlGaIn solar-blind ultraviolet detectors," *Photon. Res.* **8**, 1243–1252 (2020).
41. Y. Wang and N. Yu, "Fabrication visible-blind ultraviolet photodetector based on ZnS/GaN heterostructure with fast response," *Mater. Express* **10**, 629–633 (2020).
42. D. Guo, Z. Wu, P. Li, Y. An, H. Liu, X. Guo, H. Yan, G. Wang, C. Sun, L. Li, and W. Tang, "Fabrication of β -Ga₂O₃ thin films and solar-blind photodetectors by laser MBE technology," *Opt. Mater. Express* **4**, 1067–1076 (2014).